buildings

MDPI

Article

Dynamic Stress Path under Obliquely Incident P- and SV-Waves

Mingyuan Wang [1,2], Linfeng Song [3], Xinglei Cheng [3,*], Jianxin Zhang [3], Liqiang Lu [3] and Wenqian Li [3]

1 Powerchina Huadong Engineering Corporation Limited, Hangzhou 310014, China
2 Zhejiang Huadong Construction Engineering Corporation Limited, Hangzhou 310014, China
3 Key Laboratory of Soft Soil Engineering Character and Engineering Environment of Tianjin, Tianjin Chengjian University, Tianjin 300192, China
* Correspondence: cxl@tcu.edu.cn

Abstract: This study derives the expression of dynamic stress components of the soil element in the semi-infinite elastic space under obliquely incident P- and SV-waves, and obtained the corresponding dynamic stress path. The effects of some factors including the incidence angle, Poisson's ratio, frequency, wave velocity, phase difference, and soil depth on the dynamic stress path are analyzed. It is found that the dynamic stress path in the $(\sigma_y - \sigma_x)/2 - \tau_{xy}$ plane is an oblique ellipse, and the above factors have significant effects on that. The maximum dynamic stress level for Poisson's ratio of 0.3 is about twice that for 0.48. The maximum dynamic stress level for 2.5 Hz is about six times that for 1 Hz. In general, the maximum dynamic stress level is about 40 kPa, no matter how the wave velocity changes. Compared with other phase difference, the dynamic stress level for the phase difference of 60° is largest with a value of 43 kPa. The dynamic stress level becomes greater as the soil depth increases, and the maximum value at 30 m depth is about 40 kPa. The variation trend of the three characteristic parameters with the incident angle exhibits the double-peak or triple-peak curves for different influencing factors. The research findings can provide some guidance for the site seismic dynamic response analysis and structural seismic design.

Keywords: soil dynamics; seismic response; oblique incidence; P-wave; SV-wave

Citation: Wang, M.; Song, L.; Cheng, X.; Zhang, J.; Lu, L.; Li, W. Dynamic Stress Path under Obliquely Incident P- and SV-Waves. *Buildings* **2022**, *12*, 2210. https://doi.org/10.3390/buildings12122210

Academic Editors: Chih-Wei Lu, Meen-Wah Gui and Giuseppina Uva

Received: 16 November 2022
Accepted: 8 December 2022
Published: 13 December 2022

1. Introduction

The earthquake threat to building structures is related to the intensity of ground motion and the dynamic characteristics of the soil on the building site. Seismic wave propagation in the soil layer will result in seismic dynamic stress and then cause a complex site dynamic response (Figure 1). Previous studies have shown that the seismic dynamic response of the site depends on the dynamic stress path formed in the soil mass under incident seismic wave. Seismic waves usually include a compression wave (P-wave) and a shear wave (S-wave). At present, most studies believe that P-wave attenuates rapidly during earthquakes, so only the influence of seismic shear stress generated by vertical upward propagation (vertical incidence) of SV wave on soil dynamic response was considered [1,2]; however, some scholars have pointed out that the seismic effect caused by vertical incidence of a P-wave cannot be ignored [3–5]. In the actual seismic process, the P-wave or SV-wave is not always incident alone, and the incident direction is not always vertical; the oblique incidence of the combined two is more common. Therefore, it is very important to study the dynamic stress path of soil element under the oblique incidence of a combined P- and SV-wave and its related influencing factors for analyzing the site seismic dynamic response.

Relevant numerical simulations and experimental studies were performed for the dynamic response of soil under single incident SV-wave. Zhao et al. [6] deduced the calculation formula of the stress field for the incident SV-wave, and simulated the corresponding dynamic stress path using a hollow cylinder torsional shear apparatus. Huang et al. [7] revealed the characteristics of the dynamic stress path of the soil mass when the SV-wave is obliquely incident, and discussed the influence of the incidence angle, Poisson's ratio, wavelength, and other factors on the dynamic stress path. Hu et al. [8] studied the undrained dynamic response of soft clay under horizontal shear stress caused by the vertical incidence of SV-wave using the multi-directional cyclic simple shear apparatus. Du et al. [9] deduced the calculation formula of equivalent nodal force on artificial boundary interface for an incident SV-wave based on the explicit finite element method and viscoelastic artificial boundary conditions. You et al. [10] investigated the amplification effect of the soil layer containing the cavity in the half-space under incident SV-wave employing the indirect boundary element method. Zhao et al. [11] studied seismic dynamic responses of tunnels caused by the obliquely incident SV-wave. Wei et al. [12] investigated the impact of SV-wave incident angle on the ground motion amplification of the basin using the finite element method. Yin et al. [13] studied the amplification effect of slope topographic when subjected to obliquely incident SV-waves based on viscoelastic artificial boundary. Fu et al. [14] investigated the influence of local topographic on seismic response of tunnels subjected to obliquely incident SV-wave. Roy et al. [15] evaluated the liquefaction resistance using the Chinese dynamic cone penetration test (DPT) and shear-wave velocity measurements at eight sites in Seward and Old Valdez, Alaska. Gičev et al. [16] studied the two-dimensional translation, sway and wave motion of buildings in the process of soil–structure interaction excited by plane seismic SV-wave.

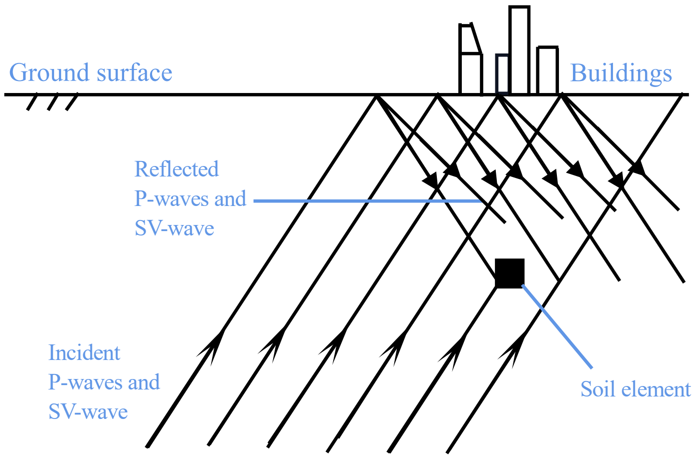

Figure 1. Diagrammatic sketch of obliquely incident seismic waves on building site.

The survey of earthquake disasters shows that P-waves can also lead to earthquake disasters that cannot be ignored, which has attracted the attention of many scholars. Huang et al. [17] revealed characteristics of the dynamic stress path when the P-wave is obliquely incident, and discussed the influence of incident angle, Poisson's ratio, and wavelength on the stress path. Cen et al. [18] analyzed the free field responses under incident P-wave employing the time-domain calculation model, and found that the dynamic response of soil layer under obliquely incidence is significantly different from that under vertical incidence. Song et al. [19] calculated seismic dynamic responses of sites under obliquely incident P-wave based on the dynamic viscoelastic artificial boundary, and found that seismic responses become more significant as the incidence angle increases. Wang et al. [20] analyzed seismic response of long-span bridges under obliquely incident P-waves, and investigated the impact of such factors as incidence angle, soil stiffness, and soil nonlinearity on the seismic responses. Liu et al. [21] analyzed seismic dynamic responses of a two-dimensional fault site under an incident P-wave and found that the incident angle, wave velocity, and frequency have certain effects on the seismic responses. Gao et al. [22] analyzed seismic responses of embankments under an obliquely incident P-wave through explicit finite element calculation. Wang et al. [23] proposed a seismic input method of an obliquely incident P-wave near field, and analyzed dynamic responses of dams. Naji et al. [24] generated an intensive series of geographic information system (GIS) maps for the seismic site classification (SSC) in Kahramanmaras city. Skarlatoudis et al. [25] estimated shallow shear-wave velocity profiles in Alaska using the initial portion of P waves from local earthquakes. Wu et al. [26] conducted an investigation into the relationship between the magnitudes of earthquakes and the properties of the first three seconds of the P waves at a single station.

In the process of earthquakes, the more common case is the oblique incidence of combined P- and SV-wave, and a few scholars have also carried out relevant research about that. Li et al. [27] simulated the oblique elliptical stress path under the oblique incidence of combined P- and SV-waves employing hollow cylinder torsional shear apparatus, and investigated dynamic characteristics of saturated sand under different stress paths. Gu et al. [28] investigated dynamic characteristics of saturated soft clay under the oblique incidence of combined P- and SV-wave by using dynamic triaxial apparatus with variable confining pressure. You et al. [29] computed seismic dynamic responses of soil layer under the oblique incidence of combined P- and SV-waves employing the accurate dynamic stiffness matrix of half-space. Pan et al. [30] proposed a random wave analysis method for the seismic response of the layered soil under the oblique incidence of combined P- and SV-waves. Sawazaki and Snieder [31] detected time-lapse changes in P- and S-wave velocities and shear wave splitting parameters associated with the 2011 Tohoku earthquake, Japan, at depths between 0 and 504 m. Liu et al. [32] investigated the scattering of elastic waves by an elastic or viscoelastic cylinder, and derived the analytical solutions of the scattered and internal fields excited by a normally incident plane P- or SV-wave. Farra and Pšenčík [33] tested alternative expressions for the P- and SV-wave moveout formulas in VTI media based on the weak-anisotropy (WA) approximation.

The above literature review indicates that most studies focus on the dynamic responses of soil mass under the incidence of a single P-wave or single SV-wave. The research on the dynamic stress path of the soil mass under oblique incidence of combined P- and SV-waves is very rare. The novelty of this study mainly has two aspects: (a) to determine the dynamic stress path by deriving the expression of dynamic stress components for soil element in the semi-infinite elastic space under the oblique incidence of combined P- and SV-waves; (b) clarify the influence law of some main factors such as incidence angle, Poisson's ratio, frequency, wave velocity, etc. on the dynamic stress path. The research findings can lay a theoretical foundation for further research on the seismic dynamic stress induced by the oblique incidence of seismic waves, and also provide some guidance for the site seismic dynamic response analysis and structural seismic design.

2. Seismic Dynamic Stress Caused by Obliquely Incident P- and SV-Waves

The calculation model is developed based on the following assumptions: the soil mass is assumed to be an elastic half-space medium, and the incident wave is a group of parallel simple harmonics with an incident angle α, as shown in Figure 2a ($\alpha = \alpha_1 = \gamma_2$). It is assumed that the wave energy does not attenuate in the process of propagation, i.e., the wave amplitude is constant and only seismic wave propagation in the plane is considered. Based on elastic wave theory [34–39], the interface between two half-spaces composed of elastic space and vacuum is called as the elastic half-space interface. Wave mode conversion will occur at the elastic interface, i.e., incident P-waves (or SV-waves) will not only generate P-Waves (or SV-waves), but will also generate SV-waves (or P-Waves) after reflection. Moreover, new waves will be generated for some specific interfaces, which leads to the complexity of elastic wave propagation. In this paper, we only study the simple case of plane harmonic wave incident on the elastic interface. The stress state of soil element below the interface caused by seismic waves is shown in Figure 2b, where σ_y is the vertical stress, σ_x is the horizontal stress, and $\sigma_x = K_0\sigma_y$ (K_0 is the coefficient of consolidation); τ_{xy} is shear stress.

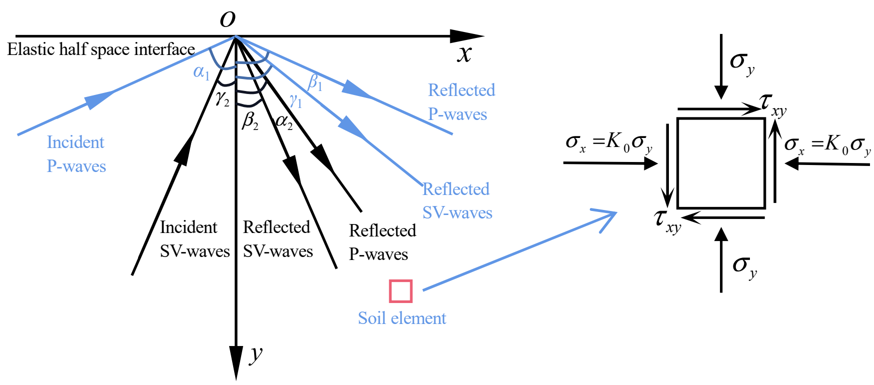

(**a**) Incident and reflected waves (**b**) Stress state of soil element

Figure 2. Diagrammatic sketch of obliquely incident P- and SV-waves on elastic half-space interface.

2.1. Calculation Formulas of Seismic Dynamic Stress

Based on the elastic wave theory, in the x-o-y plane with two-dimensional Cartesian coordinate system, the potential functions of incident P-wave and SV-wave can be recorded as [37]:

$$\phi_{-} = A_{-}^{1}\exp\left[\mathrm{ik}\left(x\sin\alpha_1 - y\cos\alpha_1 - v_p t\right)\right] \tag{1}$$

$$\psi_{-} = A_{-}^{2}\exp[\mathrm{ik}_1(x\sin\gamma_2 - y\cos\gamma_2 - v_s t)] \tag{2}$$

The potential functions of reflected P-wave and SV-wave generated by incident P-wave and SV-wave, respectively, are [37]:

$$\phi_{+}^{1} = A_{+}^{1}\exp\left[\mathrm{ik}_2\left(x\sin\beta_1 + y\cos\beta_1 - v_p t\right)\right] \tag{3}$$

$$\psi_{+}^{1} = B_{+}^{1}\exp[\mathrm{ik}_3(x\sin\gamma_1 + y\cos\gamma_1 - v_s t)] \tag{4}$$

$$\phi_{+}^{2} = B_{+}^{2}\exp\left[\mathrm{ik}_4\left(x\sin\alpha_2 + y\cos\alpha_2 - v_p t\right)\right] \tag{5}$$

$$\psi_{+}^{2} = A_{+}^{2}\exp[\mathrm{ik}_5(x\sin\beta_2 + y\cos\beta_2 - v_s t)] \tag{6}$$

Among Equations (1)–(6), ϕ_{-} and ψ_{-} are the potential function of incident P-wave and SV-wave, respectively; ϕ_{+}^{1} and ψ_{+}^{1} are the potential function of reflected P-wave and SV-wave generated by incident P-wave; ϕ_{+}^{2} and ψ_{+}^{2} are the potential function of reflected P-wave and SV-wave generated by incident SV-wave. A_{-}^{1}, A_{+}^{1}, and B_{+}^{1}, respectively, represent the amplitude of incident P-wave, and the corresponding reflected P-wave and SV-wave; A_{-}^{2}, A_{+}^{2}, and B_{+}^{2}, respectively, represents the amplitude of the incident SV-wave, and the corresponding reflected SV-wave and P-wave; The wave numbers of incident and reflected waves are $k = \omega/v_p$, $k_1 = \omega_1/v_s$, $k_2 = \omega_2/v_p$, $k_3 = \omega_3/v_s$, $k_4 = \omega_4/v_p$, $k_5 = \omega_5/v_s$, where ω, ω_1, ω_2, ω_3, ω_4, ω_5 are the corresponding circular frequencies; P-wave velocity $v_p = \sqrt{(\lambda + 2G)/\rho}$, and SV-wave velocity $v_s = \sqrt{G/\rho}$, where G and ρ are the shear modulus and mass density of soil, respectively, and λ is the Lame constant; α_1, β_1, and γ_1 are, respectively, the incident angle of P-wave and the reflection angle of the generated P-wave and SV-wave; γ_2, α_2, and β_2 are, respectively, the incident angle of the SV-wave and the reflection angle of the generated P-wave and SV-wave. In Figure 2a, the incident angle is defined as the angle between the incident direction and vertical direction (y-axis), and the reflection angle is defined as the angle between the reflected direction and vertical direction (y-axis); i presents the complex number and t represents the time.

At the ground surface, i.e., $y = 0$, the boundary conditions meet $\sigma_y = 0$, and $\tau_{xy} = 0$; therefore, one can derive that $\alpha_1 = \beta_1$, $\omega = \omega_2 = \omega_3$, $k = k_2$, Hence it can be concluded that the incident angle of incident P-wave equals to the reflection angle of the corresponding reflected P-wave, and both have the same wave number; By the same token, $\gamma_2 = \beta_2$, $\omega_1 = \omega_4 = \omega_5$, $k_1 = k_5$, similarly, the incident angle of incident SV-wave equals to the reflection angle of reflected SV-wave, and both have the same wave number. The relationship between the amplitude of incident P-wave, and corresponding reflected P-wave and SV-wave is as follows:

$$\frac{A_+^1}{A_-^1} = \frac{k^2 \sin 2\alpha_1 \sin 2\gamma_1 - k_2{}^2 \cos^2 2\gamma_1}{k^2 \sin 2\alpha_1 \sin 2\gamma_1 + k_2{}^2 \cos^2 2\gamma_1} \frac{B_+^1}{A_-^1} = \frac{2k^2 \sin 2\alpha_1 \cos 2\gamma_1}{k^2 \sin 2\alpha_1 \sin 2\gamma_1 + k_2{}^2 \cos^2 2\gamma_1} \tag{7}$$

The relationship between the amplitude of incident SV-wave, and corresponding reflected P-wave and SV-wave is as follows:

$$\frac{A_+^2}{A_-^2} = \frac{k_3{}^2 \sin 2\gamma_2 \sin 2\alpha_2 - k_5{}^2 \cos^2 2\alpha_2}{k_3{}^2 \sin 2\gamma_2 \sin 2\alpha_2 + k_5{}^2 \cos^2 2\alpha_2} \frac{B_+^2}{A_-^2} = \frac{-k_5{}^2 \sin 4\alpha_2}{k_3{}^2 \sin 2\gamma_2 \sin 2\alpha_2 + k_5{}^2 \cos^2 2\alpha_2} \tag{8}$$

Equations (7) and (8) are independent of frequency and wavelength. According to the principle of linear superposition, these two equations are valid for general time-varying waves.

According to the elastic constitutive equation (Hooke's law), geometric equation, and differential equation of motion [35,36], the dynamic stress components of any soil element under the incidence of combined P and SV-waves can be determined. When the foundation damping is not considered, the dynamic stress component is the superposition of the ones generated by the incident wave and the reflected wave.

The elastic constitutive equation is:

$$\begin{cases} \sigma_x = \lambda\left(\varepsilon_x + \varepsilon_y\right) + 2G\varepsilon_x \\ \sigma_y = \lambda\left(\varepsilon_x + \varepsilon_y\right) + 2G\varepsilon_y \\ \tau_{xy} = G\gamma_{xy} \end{cases} \tag{9}$$

where the Lame constant $\lambda = \mu E/[(1+\mu)(1-2\mu)]$, shear modulus $G = E/[2(1+\mu)]$. E is the elastic modulus, μ is Poisson's ratio, ε_x is the strain in x direction, ε_y is the strain in y direction.

The geometric equation is:

$$\begin{cases} \varepsilon_x = \frac{\partial u}{\partial x} \\ \varepsilon_y = \frac{\partial w}{\partial y} \\ \tau_{xy} = \frac{\partial u}{\partial y} + \frac{\partial w}{\partial x} \end{cases} \tag{10}$$

where u and w represent two displacement components in x and y directions, respectively.

The differential equation of motion is:

$$\begin{cases} u = \frac{\partial \phi}{\partial x} - \frac{\partial \psi}{\partial y} \\ w = \frac{\partial \phi}{\partial y} + \frac{\partial \psi}{\partial x} \end{cases} \tag{11}$$

The dynamic stress components of soil element can be determined by combining Equations (9)–(11), as represented by:

$$\begin{cases} \sigma_x & = \lambda\left[\frac{\partial^2(\phi_- + \phi_+^1)}{\partial x^2} + \frac{\partial^2(\phi_- + \phi_+^1)}{\partial y^2}\right] + 2G\left[\frac{\partial^2(\phi_- + \phi_+^1)}{\partial x^2} - \frac{\partial^2 \psi_+^1}{\partial x \partial y}\right] \\ & +\lambda\left(\frac{\partial^2 \phi_+^2}{\partial x^2} + \frac{\partial^2 \phi_+^2}{\partial y^2}\right) + 2G\left[\frac{\partial^2 \phi_+^2}{\partial x^2} - \frac{\partial^2(\psi_- + \psi_+^2)}{\partial x \partial y}\right] \\ \sigma_y & = \lambda\left[\frac{\partial^2(\phi_- + \phi_+^1)}{\partial x^2} + \frac{\partial^2(\phi_- + \phi_+^1)}{\partial y^2}\right] + 2G\left[\frac{\partial^2(\phi_- + \phi_+^1)}{\partial y^2} + \frac{\partial^2 \psi_+^1}{\partial x \partial y}\right] \\ & +\lambda\left(\frac{\partial^2 \phi_+^2}{\partial x^2} + \frac{\partial^2 \phi_+^2}{\partial y^2}\right) + 2G\left[\frac{\partial^2 \phi_+^2}{\partial y^2} + \frac{\partial^2(\psi_- + \psi_+^2)}{\partial x \partial y}\right] \\ \tau_{xy} & = G\left[2\frac{\partial^2(\phi_- + \phi_+^1)}{\partial x \partial y} - \frac{\partial^2 \psi_+^1}{\partial y^2} + \frac{\partial^2 \psi_+^1}{\partial x^2}\right] \\ & +G\left[2\frac{\partial^2 \phi_+^2}{\partial x \partial y} + \frac{\partial^2(\psi_- + \psi_+^2)}{\partial x^2} - \frac{\partial^2(\psi_- + \psi_+^2)}{\partial y^2}\right] \end{cases} \tag{12}$$

It should be noted that according to Snell's theorem [36], for the case of incident SV-wave, there is a critical incident angle β_{cr}, and $\beta_{cr} = \arcsin(\sqrt{\frac{1-2\mu}{2(1-\mu)}})$. When the incident angle of SV-wave is less than the critical incident angle, reflected P-wave, and SV-wave will be generated simultaneously; therefore, the above Equation (12) is applicable to the case that the incident angle of SV-wave is less than the critical incident angle, i.e., $\gamma_2 < \beta_{cr}$; when $\gamma_2 > \beta_{cr}$, the incident SV-wave will only generate reflected SV-wave, without the reflected P-wave; for this case, the dynamic stress component of soil element can be represented by:

$$\begin{cases} \sigma_x = \lambda\left[\frac{\partial^2(\phi_- + \phi_+^1)}{\partial x^2} + \frac{\partial^2(\phi_- + \phi_+^1)}{\partial y^2}\right] + 2G\left[\frac{\partial^2(\phi_- + \phi_-^1)}{\partial x^2} - \frac{\partial^2 \psi_+^1}{\partial x \partial y}\right] - 2G\left[\frac{\partial^2(\psi_- + \psi_+^2)}{\partial x \partial y}\right] \\ \sigma_y = \lambda\left[\frac{\partial^2(\phi + \phi_-^1)}{\partial x^2} + \frac{\partial^2(\phi + \phi_+^1)}{\partial y^2}\right] + 2G\left[\frac{\partial^2(\phi + \phi_+^1)}{\partial y^2} + \frac{\partial^2 \psi_+^1}{\partial x \partial y}\right] + 2G\left[\frac{\partial^2(\psi_- + \psi_+^2)}{\partial x \partial y}\right] \\ \tau_{xy} = G\left\{2\frac{\partial^2(\phi_- + \phi_+^1)}{\partial x \partial y} - \frac{\partial^2 \psi_+^1}{\partial y^2} + \frac{\partial^2 \psi_+^1}{\partial x^2}\right\} + G\left[\frac{\partial^2(\psi_- + \psi_+^2)}{\partial x^2} - \frac{\partial^2(\psi_- + \psi_+^2)}{\partial y^2}\right] \end{cases} \quad (13)$$

2.2. Characteristics of Dynamic Stress Path

Previous studies have shown that the dynamic stress path of soil element is elliptical under the incidence of a single P-wave or SV-wave [17]. In this study, according to Equation (12) or (13), MATLAB program is compiled to calculate the dynamic stress components, i.e., σ_x, σ_y, τ_{xy}. A typical time history for these three components is shown in Figure 3. It is found that the dynamic stress path under the incidence of combined P- and SV-wave is also usually an ellipse in $(\sigma_y - \sigma_x)/2 - \tau_{xy}$ plane as shown in Figure 4. L_a and L_b are half the length of the major axis and minor axis of the ellipse respectively, which represents the size of the ellipse; θ is the angle between the major axis and the positive horizontal axis, which represents the inclination degree of the ellipse. δ is defined as the ratio of the minor axis length to the major axis length, i.e., $\delta = L_b/L_a$, which represents the ellipticity. Obviously, δ is between 0 and 1. L_a, θ, and δ are three characteristic parameters of any inclined ellipse, which can effectively characterize the dynamic stress path of soil element.

L denotes the distance from any point on the elliptical stress path to the origin, as represented by:

$$L = \sqrt{(\frac{\sigma_y - \sigma_x}{2})^2 + \tau_{xy}{}^2} \quad (14)$$

L reflects the combined effect of normal stress difference and horizontal shear stress under complex stress path, which can represent the dynamic stress level of soil element. Obviously, when $L = L_a$, the dynamic stress level of soil element reaches the maximum. Therefore, the maximum dynamic stress level corresponding to the elliptical stress path can be characterized by L_a.

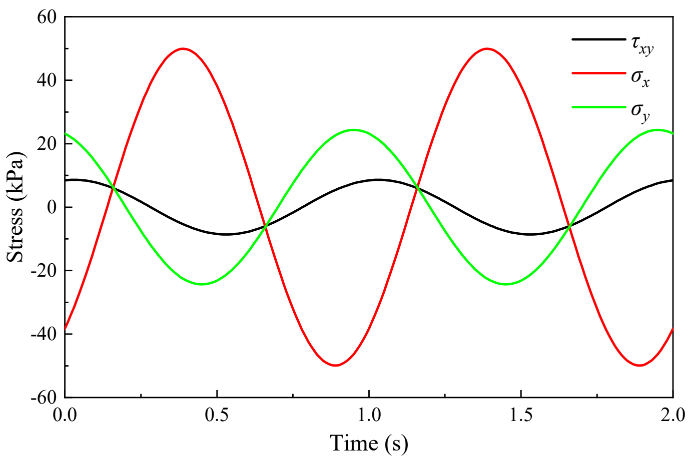

Figure 3. A typical time history for three dynamic stress components under incident P- and SV-waves ($\alpha = 30°$, $f = 1$ Hz, $\mu = 0.4$, vs. = 200 m/s, $\varphi = 0°$, $z = 10$ m; these symbols will be explained later).

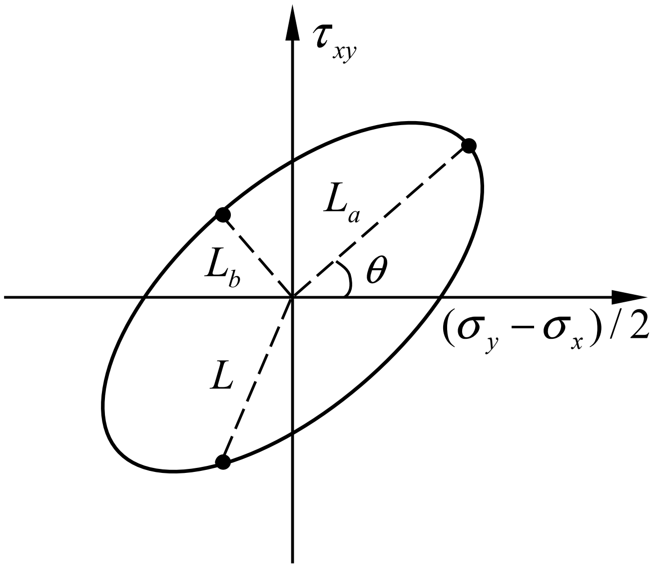

Figure 4. Geometric characteristic parameters of inclined ellipse.

3. Analysis of Factors Influencing the Dynamic Stress Path

For the oblique incidence of combined P- and SV-waves, the dynamic stress path of soil element is affected by many factors, such as the incidence angle α, Poisson's ratio μ, seismic wave frequency f, wave velocity v_s or v_p, soil depth z, and phase difference φ. Based on the three characteristic parameters: θ, δ and L_a, this chapter will discuss the influence of these factors on the elliptical stress path in detail. When calculating the dynamic stress of soil mass, the incidence angle α ranges from 0° to 90°, the soil density is 1800 kg/m^3, and the amplitude of incident wave is 1 cm.

3.1. Influence of Poisson's Ratio and Incident Angle

Relevant studies demonstrated that soils with saturation degree of more than 70% are likely to liquefy, and the corresponding liquefaction resistance is about three times that of completely saturated soils [40]. In addition, soil saturation degree depends on Poisson's ratio, and it becomes greater as the Poisson's ratio increases. When the saturation degree is between 70% and 100%, the soil Poisson's ratio is about 0.3–0.5 [41,42]; Therefore, the value of Poisson's ratio is selected in such range in this study. Other parameters in the calculation are set as: z = 10 m, v_s= 200 m/s, f = 1 Hz, $\varphi = 0$. Figure 5a–c shows the variation curves of three characteristic parameters (L_a, θ and δ) with the incidence angle α for various Poisson's ratios μ. Figure 6 shows the variation trend of the elliptical stress path with the incident angle α for various Poisson's ratios μ.

Figure 5a shows that the variation trend of L_a with α is roughly the same for various Poisson's ratios, which exhibits the double-peak curves in the overall. L_a increases gradually as α increases from 0° and reaches the first peak when α is about 30°; then, L_a decreases gradually to the minimum when α is about 45°; subsequently, L_a reaches the second peak when α is about 60°. It can be concluded that the dynamic stress level of soil element is maximum when α is about 30° and 70°, and the minimum when α is close to 90° (horizontal incidence). In general, the dynamic stress level decreases gradually as Poisson's ratio increases, and the influence of Poisson's ratio is more significant in the range of incidence angle from 30° to 80°.

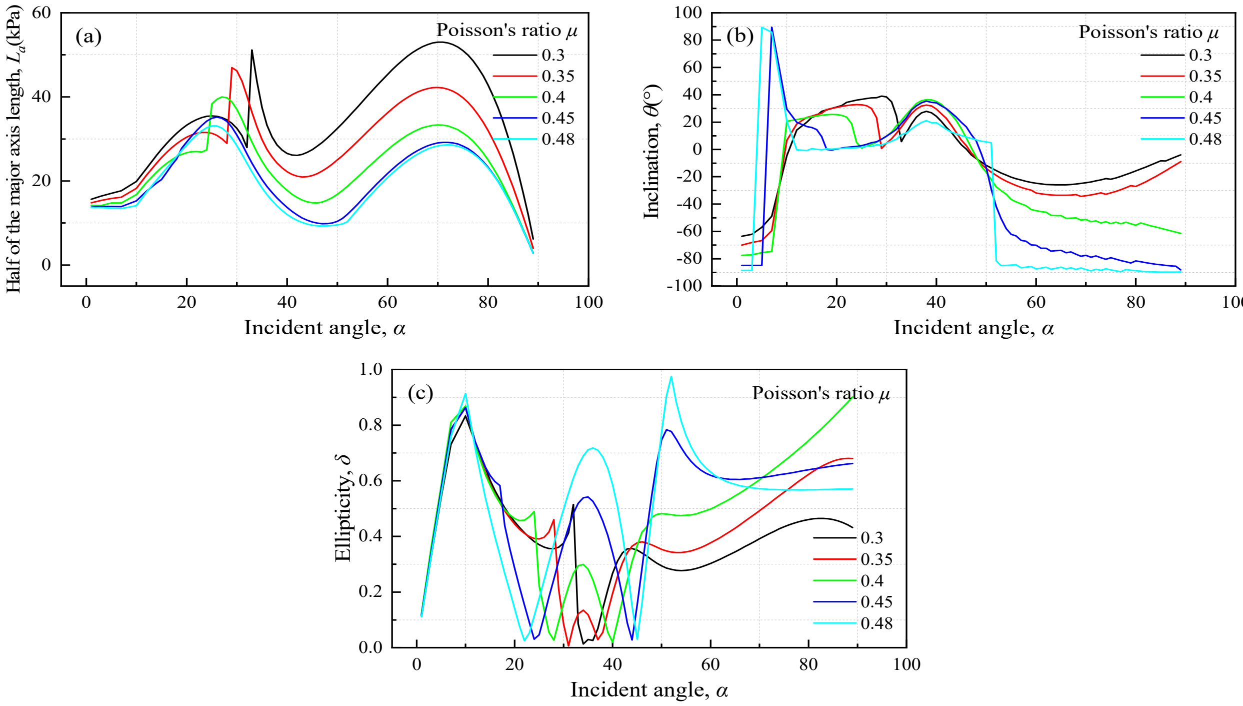

Figure 5. Variation of characteristic parameters of elliptical stress path with the incidence angle for various Poisson's ratio.

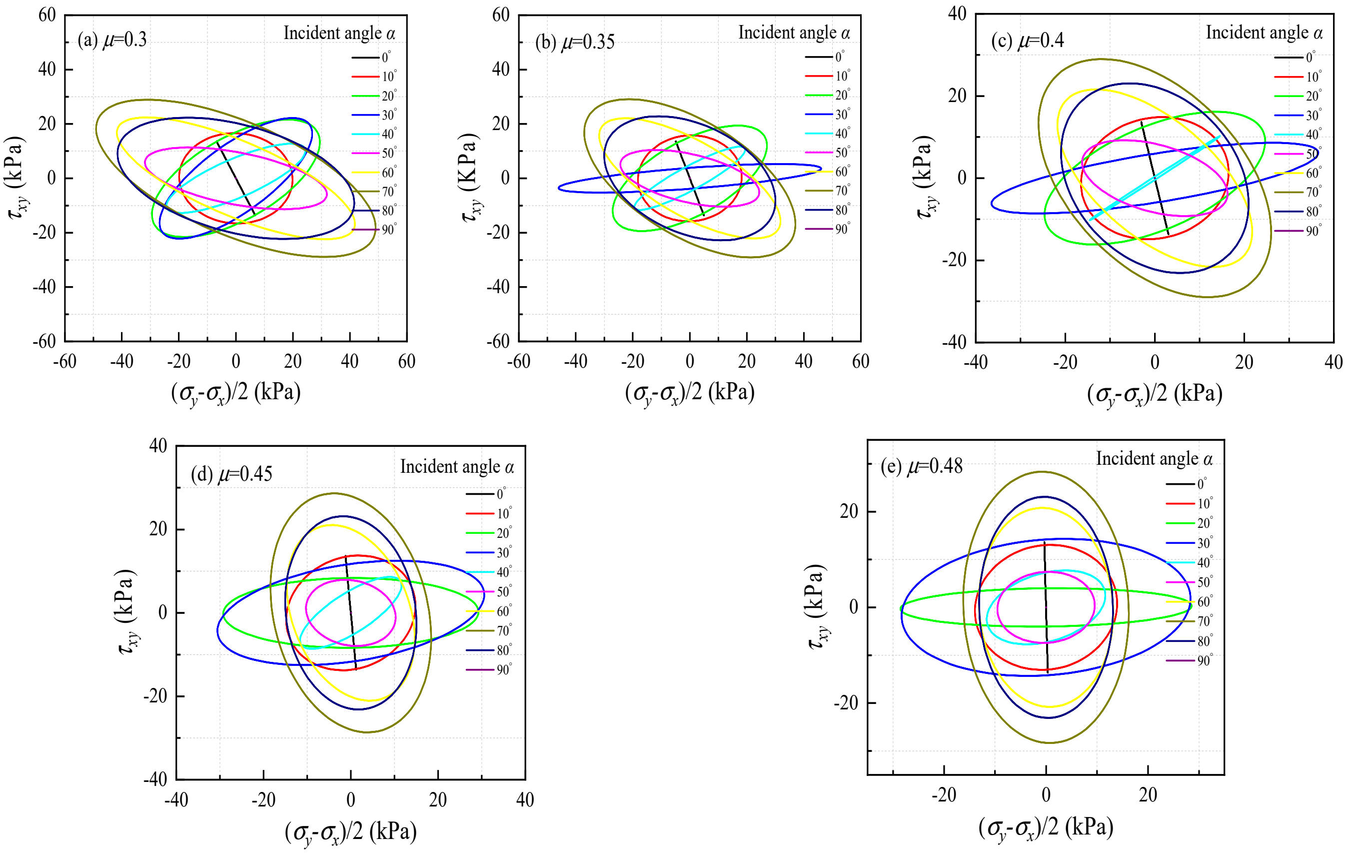

Figure 6. Variation of elliptical stress path with the incidence angle for various Poisson's ratio.

Figure 5b shows that the growth of θ is very significant when the incidence angle is within the range of 0–10° for various Poisson's ratios. Especially, when $\mu \geq 0.45$ (the soil is close to the full saturation), θ abruptly changes from the negative peak value (about $-90°$) to the positive peak value (about 90°), which indicates that the inclination angle of the elliptical stress path has undergone a sudden change, i.e., the elliptical stress path occurs severe counterclockwise rotation. This phenomenon can be observed more clearly in Figure 6, where the elliptical stress path rapidly develops from an oblique straight line (stress path for α = 0°) to an ellipse with an inclination angle of 90°. This is due to the fact that normal stress difference $\sigma_y - \sigma_x$ increases quickly while the peak shear stress τ_{xy} has insignificant change, which results in the exchange of the major axis and minor axis of the elliptical stress path. Previous research [16] revealed that the dynamic stress path is a horizontal straight line under the vertical incidence of P-wave alone (α = 0°), which is different from the stress path (oblique straight line) under the vertical incidence of combined P- and SV-waves in this study. When $\alpha \geq 50°$, Poisson's ratio has a more significant impact on θ, and the variation trend of θ with α is also different for different μ. The inclination angle (negative value) of the ellipse becomes smaller as the Poisson's ratio increases.

Figure 5c shows that the variation trend of δ with α is basically consistent for different Poisson's ratios, which exhibits a triple-peak curve in the overall trend. When α < 10°, δ increases significantly as α increases and Poisson's ratio has insignificant effect on δ. When α = 10°, δ reaches its first peak value (about 0.9). At this case, $(\sigma_y - \sigma_x)/2$ is very close to τ_{xy}, so the stress path is very close to a circle (δ = 1) as shown in Figure 6 (red color curve). The circular stress path has also been found in Huang et al.'s research about the obliquely incident P-wave [43]. When α is about 35°, δ reaches the second peak, and the peak value is greater for larger Poisson's ratio. When α is between 45° and 55°, δ reaches the third peak, and the corresponding incident angle is larger for larger Poisson's ratios. Similar to θ in Figure 5b, Poisson's ratio has a significant impact on δ when $\alpha \geq 50°$.

3.2. Influence of Frequency and Incident Angle

Relevant studies found that the dominant frequency of earthquakes with magnitude of 5–8 is usually 0.5–2.5 Hz [44]; hence, the influence of the frequency on dynamic stress path is discussed in such range of frequency herein. Other parameters in the calculation are set as: z = 10 m, v_s = 200 m/s, $\mu = 0.4$, φ = 0. Figure 7 shows the variation curves of three characteristic parameters with the incidence angle for various frequencies. Figure 8 shows the variation trend of the elliptical stress path with the incident angle for various frequencies.

Figure 7a shows that L_a decreases non-monotonically as α increases in the overall for various frequencies. L_a reaches the peak value twice when α is about 30° and 70°, respectively. For the same α, L_a is greater for higher frequency and the increase in L_a is more significant as the frequency increases, which demonstrates that the wave frequency has significant influence on the dynamic stress level of soil element. This is consistent with Huang et al.'s findings under the incidence of single P-wave [7]. The dynamic stress level increases as the frequency increases, and the rate of increase is different for different α. In the case of vertical incidence (α = 0°), the stress path is an oblique straight line as shown in Figure 8, and the length of the straight line increases significantly as the frequency increases; in the case of horizontal incidence (α = 90°), the dynamic stress level tends to be 0, so the stress path tends to be a point.

Figure 7b shows that the variation trend of θ with α exhibits double-peak curves in the overall for various frequencies. When α < 20°, θ increases significantly with α, and the frequency has a significant impact on θ; θ has an abrupt change from negative peak to positive peak, and the change is more significant for greater frequencies. This indicates that the elliptical stress path has a sharp counterclockwise rotation, which can be observed more clearly in Figure 8. θ reaches the second peak at about 40° and then gradually decreases. Previous research has revealed that the frequency had a great influence on the inclination angle of elliptical stress path under the incidence of single P-wave or SV-wave [7,17]. The present research demonstrates that this conclusion has some limitations for the oblique incidence of combined P- and SV-waves. It is worth noting that when the incidence angle is within the range of 25–40° and more than 60°, the effect of the frequency on the inclination angle of the elliptical stress path is insignificant.

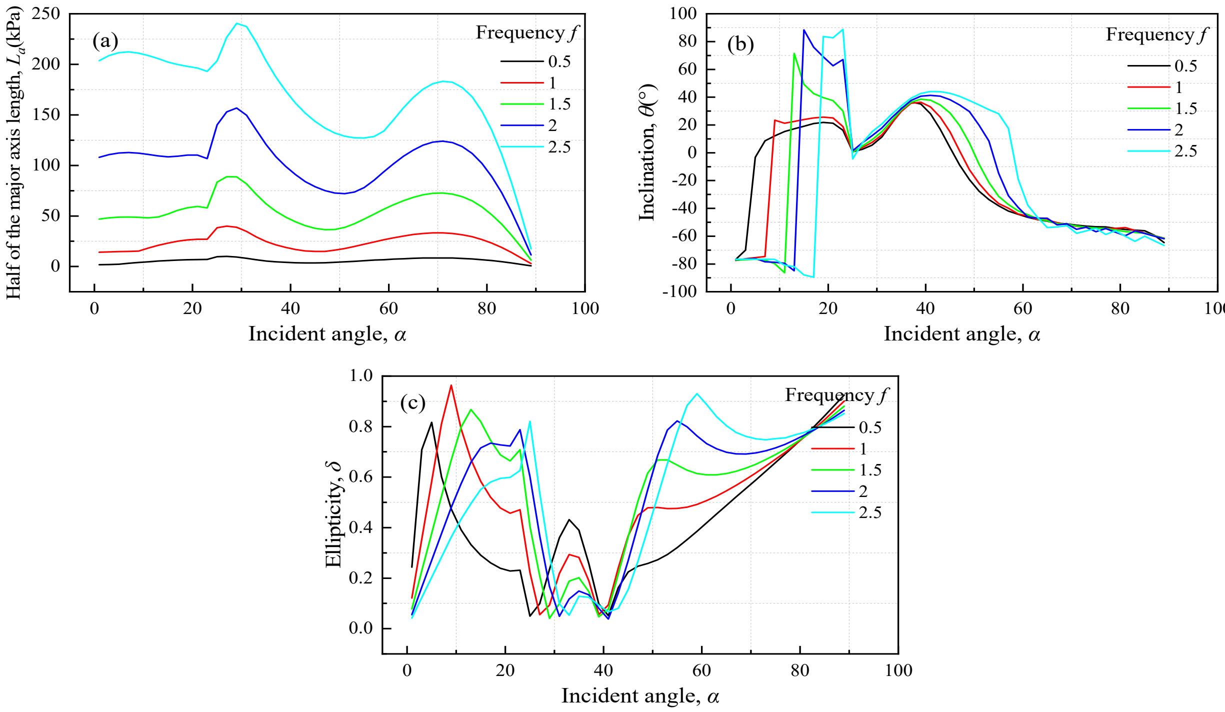

Figure 7. Variation of characteristic parameters of elliptical stress path with the incidence angle for various frequencies.

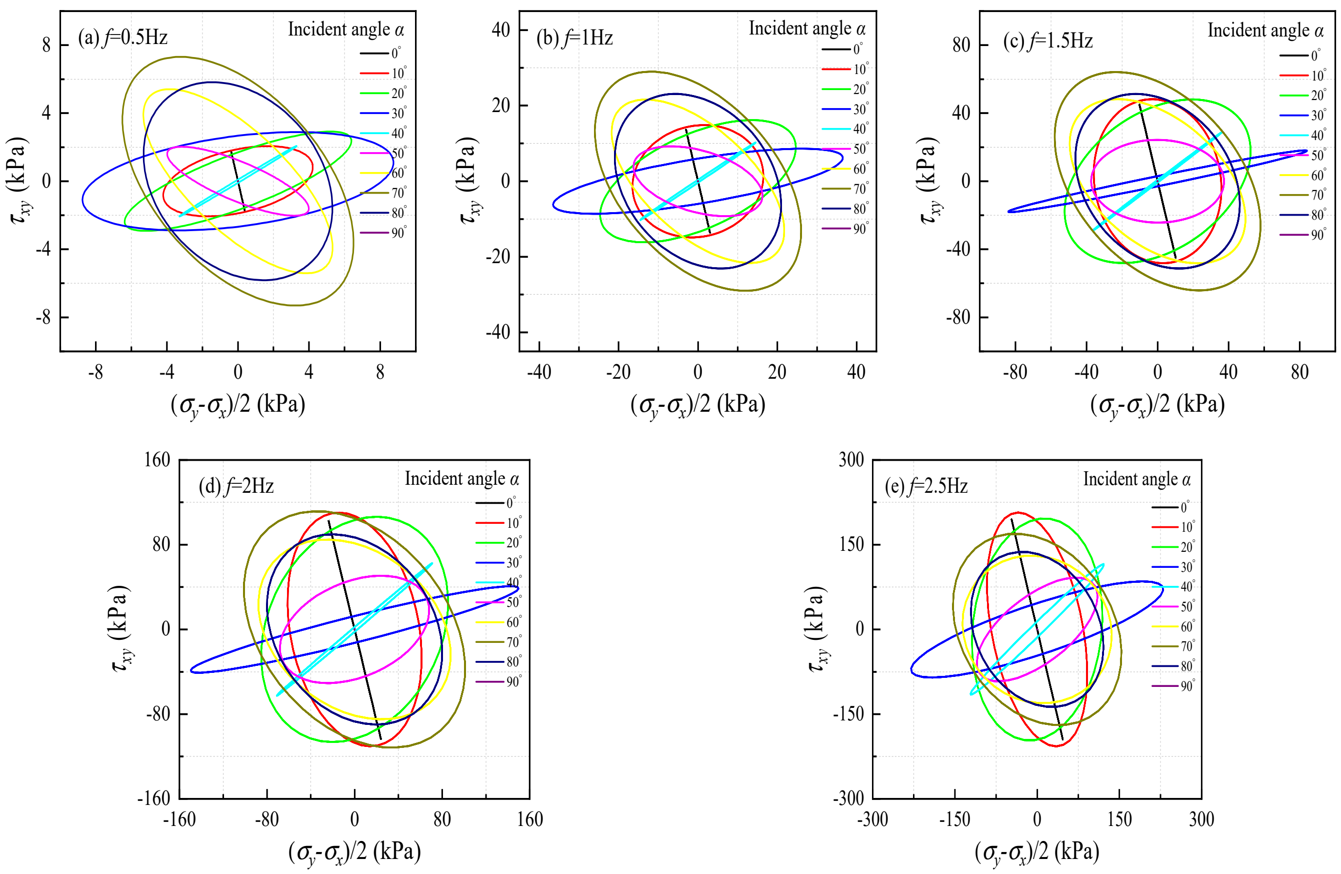

Figure 8. Variation of elliptical stress path with the incidence angle for various frequencies.

Figure 7c shows the variation trend of δ with α exhibits triple-peak curves in the overall for various frequencies, and the frequency has a significant impact on δ. δ reaches the first peak value when α is within the range of 0–30°. The incident angle corresponding to the peak value is larger for higher frequency; however, the peak value does not increase monotonously as the frequency increases. δ reaches the second peak when α is within the range of 30–40°, and the peak value is greater for lower frequency. δ reaches the third peak when α is within the range of 40–70°, and the peak value as well as the corresponding incidence angle is greater for higher frequency. The frequency has little effect on δ when α is within the range of 80–90° (close to horizontal incidence).

3.3. Influence of Wave Velocity and Incident Angle

Previous studies have demonstrated that the depth of soil liquefaction is usually within 30 m, and the corresponding shear-wave velocity is about 100 m/s–480 m/s [44–46]; hence, the influence of wave velocity v_s on soil dynamic stress path is investigated in the range of 100 m/s–600 m/s. Other parameters in the calculation are set as: z = 10 m, f = 1 Hz, $\mu = 0.4$, $\varphi = 0$. Figure 9 shows the variation curves of three characteristic parameters with the incidence angle for various wave velocities. Figure 10 shows the variation trend of the elliptical stress path with the incident angle for various velocities.

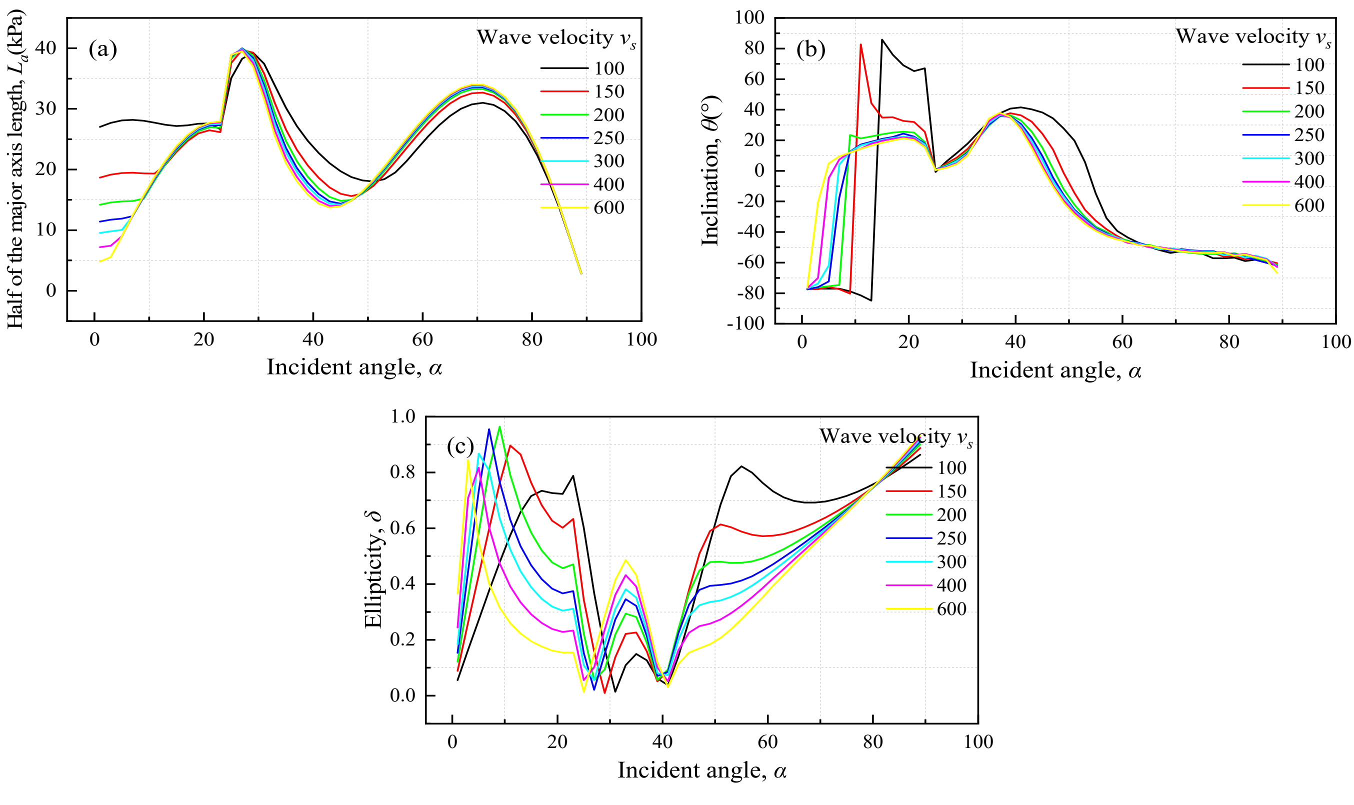

Figure 9. Variation of characteristic parameters of elliptical stress path with the incidence angle for various wave velocity.

Figure 9a shows that the variation trend of L_a with α exhibits double-peak curves in the overall for various velocities. Compared with the influence of frequency in Figure 7a, the influence of wave velocity is insignificant. L_a increases insignificantly as α increases when α is small for various v_s. L_a is almost the same for different velocity when α reaches 25°, and then follows almost the same growth trend until reaching the first peak value when α is about 30°. Subsequently, L_a gradually decreases and reaches the minimum value when α is about 45°. L_a reaches the second peak value when α is about 70°. The wave velocity has little influence on L_a in the overall. Relevant research demonstrated that the change in wave velocity had little impact on the dynamic stress level of soil element under the incidence of single P-wave [7,17], which is consistent with the present conclusion for the oblique incidence of combined P- and SV-waves. However, previous studies have not given dynamic stress paths at different wave velocities.

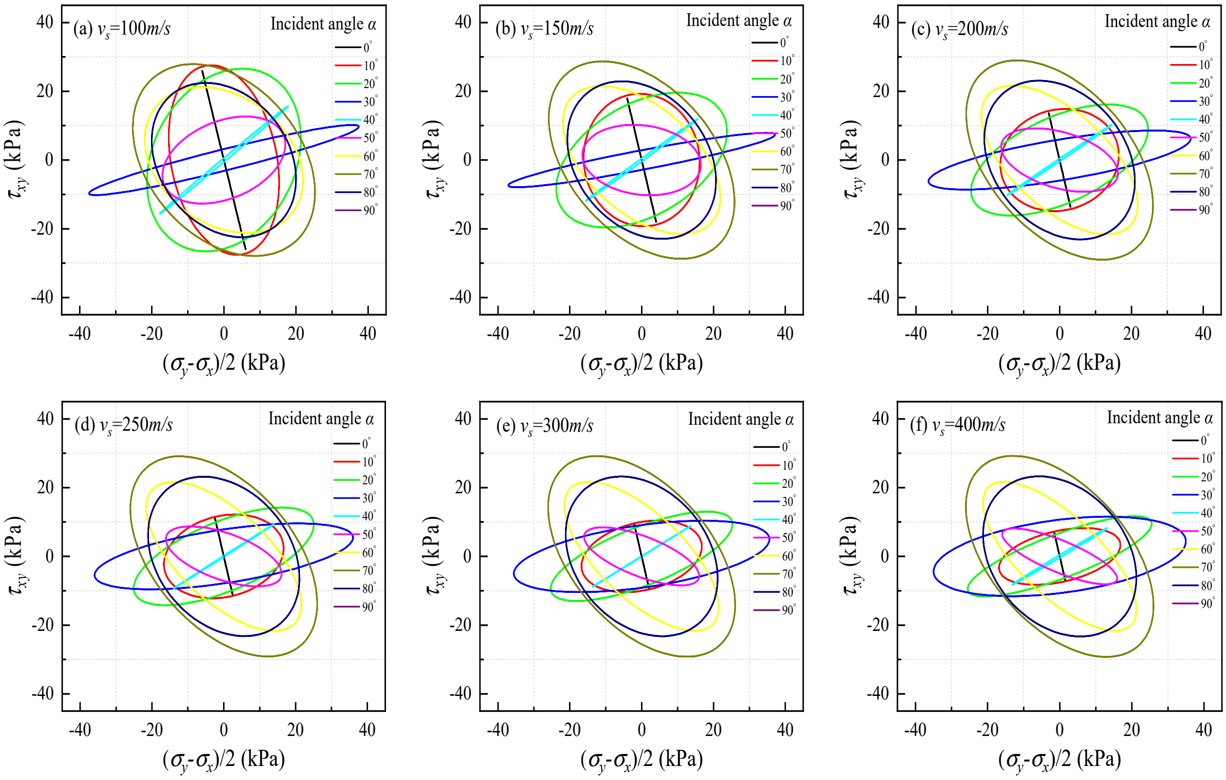

Figure 10. Variation of elliptical stress path with the incidence angle for various wave velocity.

Figure 9b shows that the variation trend of θ with α for various v_s is similar to that for various f as shown in Figure 7b. The wave velocity has a significant impact on θ when $\alpha < 20°$; in such range, θ will abruptly change and reach the positive peak, and the peak value is greater for smaller wave velocity. The significant rotation of the elliptical stress path when θ abruptly changes can be observed in Figure 10. During the rotation process, the peak value of τ_{xy} has insignificant change, but $\sigma_y - \sigma_x$ increases rapidly, which results in the exchange of the major axis and minor axis of the elliptical stress path. When α is in the range of 40–60°, the wave velocity has a certain influence on θ, and θ is larger for smaller wave velocity. When α is between 25° and 40° or larger than 60°, the influence of wave velocity on θ is very insignificant.

Figure 9c shows that the variation trend of δ with α for various v_s is similar to that for various f as shown in Figure 7c. Wave velocity has a significant effect on δ. δ reaches the first peak value when α is between 0° and 30°, and the corresponding α is greater for smaller wave velocity. δ reaches the second peak value when α is within the range of 30–40°, and the peak value is greater for higher wave velocity. δ reaches the third peak value when α is within the range of 40–70°, and the peak value and the corresponding incidence angle is larger for smaller wave velocity. The influence of wave velocity on δ is insignificant when α is between 80–90° (close to horizontal incidence).

3.4. Influence of Phase Difference and Incident Angle

The incident P-wave and SV-wave usually have different phase differences. To the author's knowledge, the effect of phase difference on the dynamic stress path has not been studied in the existing literature. In this study, the phase differences are selected as 0°, 45°, 60°, 90°, 135° and 180° respectively to discuss its influence on soil dynamic stress path. Other parameters in the calculation are set as: z = 10 m, f = 1 Hz, v_s = 200 m/s, μ = 0.4.

Figure 11 shows the variation curves of three characteristic parameters with the incidence angle for various phase differences. Figure 12 shows the variation trend of the elliptical stress path with the incident angle for various phase difference.

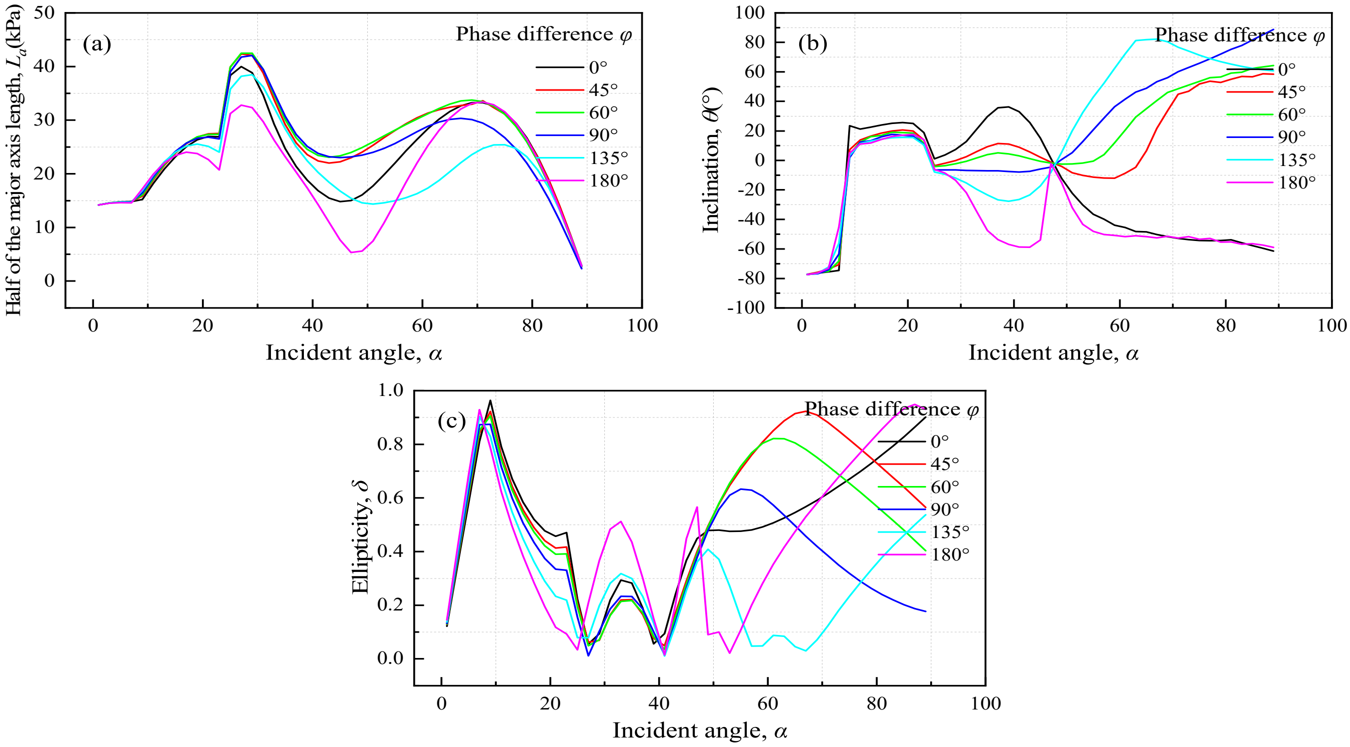

Figure 11. Variation of characteristic parameters of elliptical stress path with the incidence angle for various phase differences.

Figure 11a shows that the variation trend of L_a with α exhibits double-peak curves in the overall for various phase difference. L_a almost does not change as α increases until $\alpha > 10°$. However, the phase difference has little effect on L_a when $\alpha < 20°$; L_a reaches the first peak value when α approaches to 28°, and then gradually decreases. L_a reaches the minimum value when α is within the range of 40–50°, and L_a corresponding to 180° is the minimum for different phase difference. L_a reaches the second peak value when α is about 70°. In general, the phase difference has insignificant effect on L_a when α is small (close to horizontal incidence) or α is large (close to vertical incidence), while it has greater effect on L_a under the normal oblique incidence.

Figure 11b shows that the variation trend of θ with the incidence angle under different phase difference φ is quite different. θ increases sharply as α increases when $\alpha < 10°$; however, the increase is insignificant when $\alpha > 10°$. In general, the impact of phase difference on θ is insignificant when α is within the range of 0–25°. θ reaches an extreme value when α is about 40°; however, the extreme value corresponding to different phase differences are different; the extreme value of θ is positive when $\varphi < 90°$ and reaches the maximum when $\varphi = 0°$; the extreme value of θ is negative when $\varphi > 90°$ and reaches the minimum when $\varphi = 180°$. It demonstrates that as the phase difference gradually increases, the elliptical stress path gradually rotates clockwise from positive 40° inclination to negative 60° inclination, which can be more clearly observed in Figure 12. The variation trend of θ with α for different φ is significantly different when $\alpha > 50°$; θ decreases as α increases when $\varphi < 60°$, while θ increases as α increases when $\varphi \geq 60°$.

Figure 11c shows that the variation trend of δ with α exhibits triple-peak curves in the overall for various phase differences. When $\alpha < 10°$, δ increases sharply as α increases, and the influence of φ on δ is insignificant. δ reaches the first peak when α is about 10° for different φ. δ reaches the second peak value when α is within the range of 30–40°, and the peak value has a maximum when φ = 180°, but the peak value does not change monotonously with φ. δ reaches the third peak value when α is within the range of 40–70°; in such range, φ has a very significant effect on δ, and the variation trend of δ with α is different for different φ.

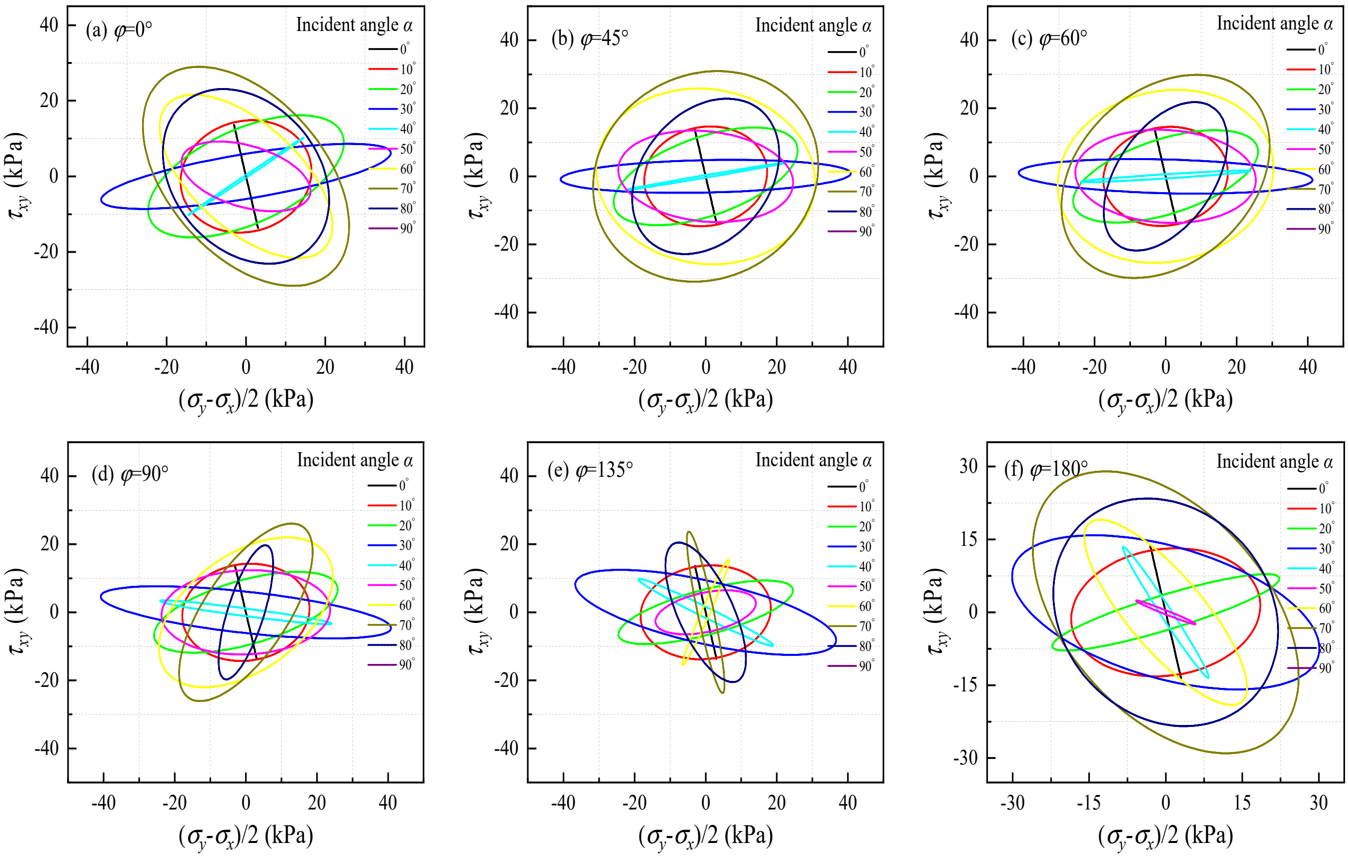

Figure 12. Variation of elliptical stress path with the incidence angle for various phase difference.

3.5. Influence of Soil Depth and Incident Angle

The dynamic stress state of soil element at different depths is different under the combined incidence of P- and SV-waves. Since soil liquefaction usually occurs within 30 m depth [47], the range of soil depth from 0 m to 30 m is selected, and different incidence conditions are set: (a) approximate vertical incidence (α = 1°, 5° and 9°); (b) oblique incidence (α = 15°, 45° and 60°); (c) approximate horizontal incidence (α = 80°, 85° and 89°), then the influence of soil depth z on dynamic stress path under different incident conditions is discussed. Other parameters in the calculation are set as: f = 1 Hz, v_s = 200 m/s, $\mu = 0.4$, $\varphi = 0$. Figure 13 shows the dynamic stress path of soil element under different incident angles and soil depth.

Figure 13a shows that the stress path is an oblique straight line when z = 0 in the case of approximate vertical incidence. τ_{xy} increases more significantly than $\sigma_y - \sigma_x$ as z increases; therefore, the elliptical stress path becomes more slender in the vertical. As the incident angle increases, τ_{xy} has an insignificant change at the same depth, but $\sigma_y - \sigma_x$ gradually increases; therefore, the inclination angle θ of the ellipse stress path has insignificant change, but its shape gradually becomes 'fat' in the transverse direction, which indicates that the dynamic stress level of the soil element gradually increases. This phenomenon can be attributed to the fact that the increase in incident angle causes the rapid growth of σ_y, while other stress components have insignificant changes.

In the case of oblique incidence, when the soil depth z = 0, the stress path is an oblique straight line (a horizontal straight line for 45°) when α = 15° and 45°, but an ellipse when α = 60°, as shown in Figure 13b. When α = 15°, as the soil depth increases, τ_{xy} increases significantly, but $\sigma_y - \sigma_x$ decreases slightly, so the inclination angle of the ellipse gradually increases with counterclockwise rotation, and the elliptical shape becomes more 'fat'. When α = 45°, τ_{xy} increases more significantly than $\sigma_y - \sigma_x$, the elliptical stress path rotates counterclockwise, and the elliptical shape is generally "slender". When α = 60°, the peak value of $\sigma_y - \sigma_x$ and τ_{xy} do not change significantly as the soil depth increases, but the ratio of the minor axis length to the major axis length δ gradually increases, so the shape of the ellipse becomes more "fat" with insignificant changes of inclination angle θ. Compared with the approximate vertical incidence as shown in Figure 13a, the change in elliptical stress path with soil depth and incidence angle under oblique incidence is more complex.

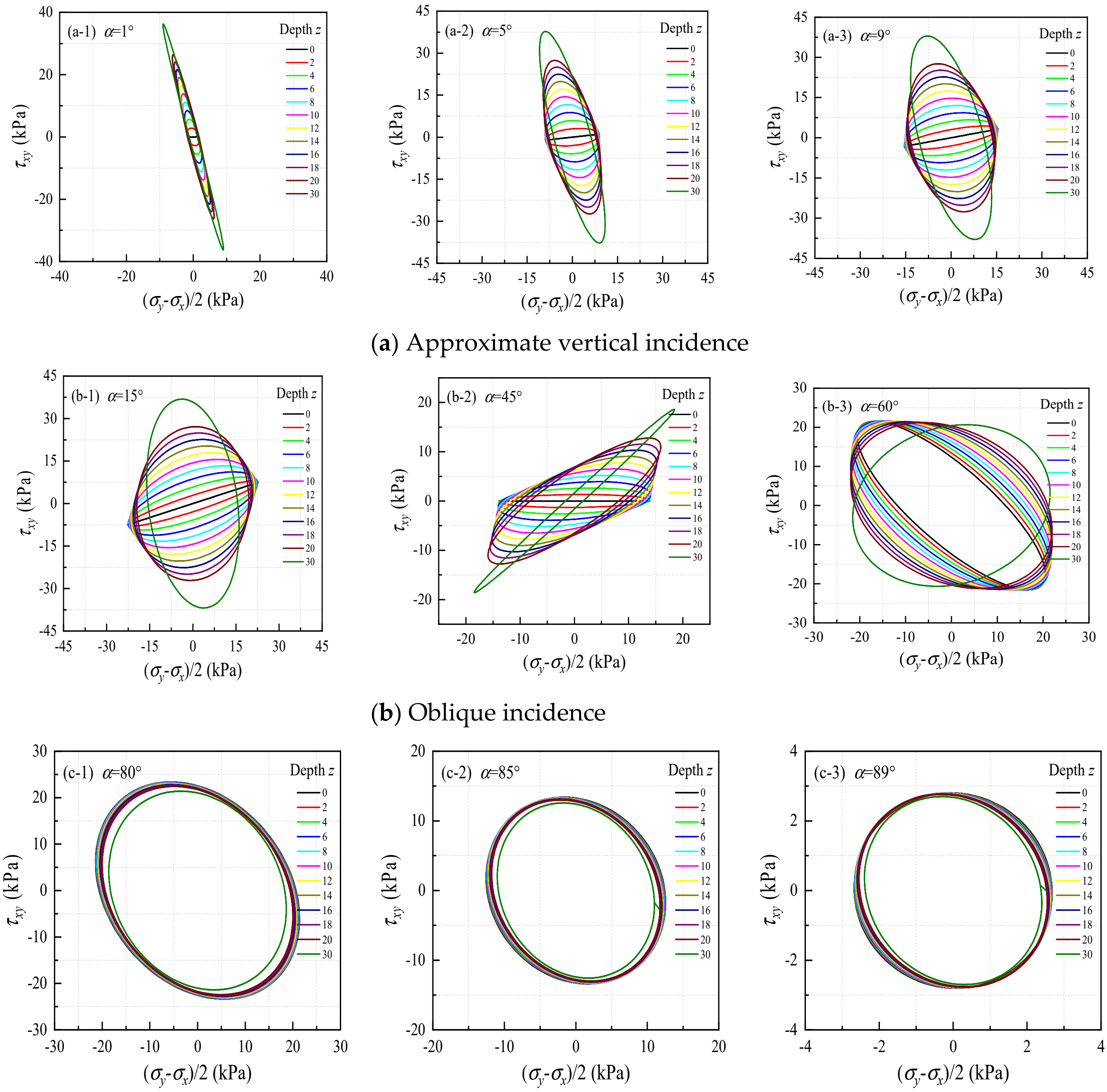

(**a**) Approximate vertical incidence

(**b**) Oblique incidence

(**c**) Approximate horizontal incidence

Figure 13. Variation of elliptical stress path with the soil depth for different incidence conditions.

In the case of approximate horizontal incidence as shown in Figure 13c, the influence of soil depth on the shape of elliptical stress path is insignificant. Both $\sigma_y - \sigma_x$ and τ_{xy}

decrease significantly as the incident angle increases, which indicates that the dynamic stress level of the soil element decreases significantly. Previous research revealed that the dynamic stress level becomes greater as the soil depth increases for the incidence of single P-wave or SV-wave [7,17]. This conclusion has some limitations for the oblique incidence of combined P- and SV-waves in this study. It should be noted that the dynamic stress level increases as the soil depth increases at most incident angles, but the effect of soil depth on the dynamic stress level is insignificant when approaching horizontal incidence.

4. Conclusions

(1) This study derives the expression of dynamic stress components of soil element in the semi-infinite elastic space under obliquely incident P- and SV-waves, and obtains the corresponding dynamic stress path. It is found that the dynamic stress path of the soil element in $\left(\sigma_y - \sigma_x\right)/2 - \tau_{xy}$ plane is usually an oblique ellipse.

(2) The variation trend of L_a with the incidence angle α exhibits double-peak curves for various Poisson's ratio μ. L_a decreases gradually as μ increases. The maximum dynamic stress level for Poisson's ratio of 0.3 is twice that for 0.48, the inclination angle of the elliptical stress path has an abrupt change when the soil is close to the full saturation. μ has a more significant impact on the inclination angle when $\alpha \geq 50°$. The variation trend of δ with α exhibits a triple-peak curve for different μ, and the peak value is greater for larger μ in the overall trend.

(3) L_a is greater for higher wave frequency at the same incident angle α, which demonstrates that the dynamic stress level of soil element is greater with higher frequency. The dynamic stress level for 0.5 Hz approaches zero, and the maximum dynamic stress level for 2.5 Hz is about 6 times that for 1 Hz. When $\alpha < 20°$, θ increases significantly with α, and the frequency has a significant impact on θ; in this range of incidence angle, θ has an abrupt change from negative peak to positive peak. The variation trend of δ with α exhibits triple-peak curves in the overall for various frequencies, and the frequency has a significant impact on δ.

(4) The variation trend of L_a with α exhibits double-peak curves in the overall for various wave velocities v_s. Compared with the wave frequency, the influence of wave velocity on L_a is insignificant. The variation trend of θ with α for various v_s is similar to that for various frequency, and θ is larger for smaller v_s. The variation trend of δ with α exhibits triple-peak curves in the overall for various v_s, and v_s has a significant effect on δ. In general, the maximum dynamic stress level is about 40 kPa no matter how v_s changes.

(5) The phase difference φ has less effect on L_a for approximate horizontal or vertical incidence, while it has greater effect on L_a under normal oblique incidence. The variation trend of θ with the incidence angle under different φ is quite different. θ reaches the second extreme value when α is about 40°, and the extreme value is greater for smaller φ. The influence of φ on δ is insignificant when $\alpha < 10°$, but the influence is very significant when α is within the range of 40–70°. In general, compared with other phase difference, the dynamic stress level for the phase difference of 60° is largest with a value of 43 kPa.

(6) In the case of approximate vertical incidence, the elliptical stress path becomes more vertically slender as the soil depth increases, and the dynamic stress level of soil element gradually increases as the incident angle increases. The change in elliptical stress path becomes more complex in the case of oblique incidence. In the case of approximate horizontal incidence, the influence of soil depth on the elliptical stress path is insignificant, and the dynamic stress level of soil element decreases significantly as the incident angle increases. The dynamic stress level becomes greater as the soil depth increases, and the maximum dynamic stress level at 30 m depth is about 40 kPa.

Author Contributions: Methodology, M.W., L.S. and X.C.; software, L.S.; validation, J.Z.; investigation, X.C.; resources, M.W.; data curation, M.W.; writing—original draft preparation, L.S.;

writing—review and editing, W.L.; visualization, L.L.; supervision, J.Z.; project administration, L.L.; funding acquisition, X.C. All authors have read and agreed to the published version of the manuscript.

Funding: This work was supported by the National Natural Science Foundation of China (52108334), the Natural Science Foundation of Tianjin City (20JCYBJC00570), and the Science and Technology Projects of Powerchina Huadong Engineering Corporation Limited (KY2020-KC-08-01-2021).

Data Availability Statement: The data presented in this study are available on request from the corresponding author. The data are not publicly available due to the follow-up research.

Conflicts of Interest: The authors declare no conflict of interest.

Nomenclature

A_-^1	Amplitude of incident P-wave
A_+^1	Amplitude of reflected P-wave induced by incident P-wave
A_-^2	Amplitude of incident SV-wave
A_+^2	Amplitude of reflected SV-wave induced by incident SV-wave
B_+^1	Amplitude of reflected SV-wave induced by incident P-wave
B_+^2	Amplitude of reflected P-wave induced by incident SV-wave
E	Elastic modulus
f	Wave frequency
G	Shear modulus
i	Complex number
k	Wave numbers
K_0	Coefficient of consolidation
L	Distance from any point on the elliptical stress path to the origin
L_a	Half of the major axis length
L_b	Half of the minor axis length
t	Time
u	Displacement components in x direction
v_p	P-wave velocity
v_s	Shear-wave velocity
v_{SV}	SV-wave velocity
w	Displacement components in y direction
z	Soil depth
α	Incidence angle
α_1	Incident angle of P-wave
α_2	Reflection angle of P-wave induced by incident SV-wave
β_1	Reflection angle of P-wave induced by incident P-wave
β_2	Reflection angle of SV-wave induced by incident SV-wave
β_{cr}	Critical incident angle
γ_1	Reflection angle of SV-wave induced by incident P-wave
γ_2	Incident angle of SV-wave
δ	Ellipticity
ε_x	Strain in x direction
ε_y	Strain in y direction
θ	Inclination angle
λ	Lame constant
μ	Poisson's ratio
σ_y	Vertical stress (y direction)
σ_x	Horizontal stress (x direction)
ρ	Mass density of soil
τ_{xy}	Shear stress
ϕ_-	Potential function for incident P-wave
ϕ_+^1	Potential function for reflected P-wave induced by incident P-wave
ϕ_+^2	Potential function for reflected P-wave induced by incident SV-wave
ψ_-	Potential function for incident SV-wave

ψ_+^1 Potential function for reflected SV-wave induced by incident P-wave
ψ_+^2 Potential function for reflected SV-wave induced by incident SV-wave
φ Phase difference
ω Circular frequencies

References

1. Seed, H.B.; Idriss, I.M. Simplified procedure for evaluating soil liquefaction potential. *J. Soil Mech. Found. Div. Am. Soc. Civ. Eng. ASCE.* **1971**, *97*, 1249–1273. [CrossRef]
2. Seed, H.B.; Idriss, I.M.; Arango, I. Evaluation of liquefaction potential using field performance data. *J. Geotech. Geoenviron. ASCE.* **1983**, *109*, 458–482. [CrossRef]
3. Jin, X.; Liao, Z.P. Statistical research on S-wave incident angle. *Annu. Disas. Prev. Res. Inst.* **1997**, *40*, 91–97.
4. Wu, C.S.; Yu, T.T.; Peng, W.F.; Ye, Y.T.; Lin, S.S. Site response variation due to the existence of near-field cracks based on strong motion records in the Shi-Wen river valley, southern Taiwan. *J. Geophys. Eng.* **2014**, *11*, 055002. [CrossRef]
5. Sigaki, T.; Kiyohara, K.; Sono, Y.; Kinosita, D.; Masao, T.; Tamura, R.; Yoshimura, C.; Ugata, T. Estimation of earthquake motion incident angle at rock site. In Proceedings of the 12th World Conference Earthquake Engineering, Upper Hutt, New Zealand, 30 January–4 February 2000.
6. Zhao, R.B.; Bi, M.; Zhang, Y.; Liu, Z.X.; Wu, Z.Y. Half-space SV wave oblique incidence stress path in soil and hollow cylinder dynamic torsional shear test simulation. *World Earthq. Eng.* **2016**, *32*, 231–238.
7. Huang, B.; Li, Q.Q.; Ling, D.S.; Wang, Y. Analysis of dynamic stress path due to oblique incidence of SV-waves and its influencing factors. *J. Vib. Shock* **2018**, *37*, 6–16.
8. Hu, X.Q.; Wang, H.; Fu, H.T.; Liu, F.Y. Effects of bidirectional unconstant amplitude shear stress on dynamic properties of soft clay in under ellipse stress path. *J. Southeast Univ. Engl. Ed.* **2019**, *49*, 433–439.
9. Du, X.L.; Huang, J.Q.; Zhao, M.; Jin, L. Effect of oblique incidence of SV waves on seismic response of portal sections of rock tunnels. *J. Geotech. Eng.* **2014**, *36*, 1400–1406.
10. You, H.B.; Liang, J.W. Scattering of plane SV waves by a cavity in a layered half-space. *Rock Soil Mech.* **2006**, *27*, 383–388.
11. Zhao, X.; Zhang, C.M.; Du, X.L.; Huang, J.Q.; Zhao, M. The analysis of the seismic response of mountain tunnels under SV waves with different incident directions. *J. Vib. Eng. Technol.* **2018**, *31*, 698–706.
12. Wei, C.Q.; Yu, Y.Y.; Ding, H.P. Study on amplification characteristics of ground motion in layered basin in time and frequency domain under oblique incidence of SV wave. *Earthq. Eng. Eng. Vib.* **2022**, *42*, 225–234.
13. Yin, C.; Li, W.H.; Zhao, C.G. Research of slope topographic amplification subjected to obliquely incident SV-waves. *J. Vib. Acoust.* **2020**, *33*, 971–984.
14. Fu, F.; Zhao, C.G.; Li, W.H.; Zhang, W.H. Influence of local topographic on seismic response of tunnels subjected to obliquely incident SV waves. *J. Beijing Jiaotong Univ.* **2012**, *36*, 79–84.
15. Roy, J.; Rollins, K.M.; Athanasopoulos-Zekkos, A.; Harper, M.; Linton, N.; Basham, M.; Zekkos, D. Gravel liquefaction assessment using dynamic cone penetration and shear wave velocity tests based on field performance from the 1964 Alaska earthquake. *Soil Dyn. Earthq. Eng.* **2022**, *160*, 107357. [CrossRef]
16. Gičev, V.; Trifunac, M.D.; Orbović, N. Two-dimensional translation, rocking, and waves in a building during soil-structure interaction excited by a plane earthquake SV-wave pulse. *Soil Dyn.* **2016**, *88*, 76–91. [CrossRef]
17. Huang, B.; Li, Q.Q.; Ling, D.S.; Liu, J.W.; Wang, Y. Analysis of the dynamic stress path under obliquely incident P-waves and its influencing factors. *J. Zhejiang Univ. Sci. A* **2017**, *18*, 776–792. [CrossRef]
18. Cen, W.J.; Du, X.H.; Li, D.J.; Yuan, L.N. Oblique Incidence of Seismic Wave Reflecting Two Components of Design Ground Motion. *Shock Vib.* **2018**. [CrossRef]
19. Song, Z.Q.; Wang, F.; Li, Y.L.; Liu, Y.H. Nonlinear seismic responses of the powerhouse of a hydropower station under near-fault plane P-wave oblique incidence. *Eng. Struct.* **2019**, *199*, 109613. [CrossRef]
20. Wang, D.G.; Shi, P.X.; Zhao, C.G. Two-dimensional in-plane seismic response of long-span bridges under oblique P-wave incidence. *Bull. Earthq. Eng.* **2019**, *17*, 5073–5099. [CrossRef]
21. Liu, B.D.; Yu, M.; Wang, W.; Zhou, Z.H.; Li, X.J. Influence of Fault Parameters on Ground Motion under Incident P Waves. *J. Earthq. Eng.* **2017**, *39*, 160–167.
22. Gao, X.J.; Qian, H.; Guo, Y.C.; Wang, F. Seismic response analysis of GRPS embankment under oblique incident P wave. *J. Cent. South Univ.* **2016**, *23*, 721–728. [CrossRef]
23. Wang, M.H.; Chi, S.C. Dynamic response analysis of high earth-rockfill dam subjected to P wave with arbitrary incoming angles. *Soil Dyn. Earthq. Eng.* **2022**, *157*, 107260. [CrossRef]
24. Naji, D.M.; Akin, M.K.; Cabalar, A.F. A comparative study on the V_{S30} and N_{30} based seismic site classification in Kahramanmaras, Turkey. *Adv. Civ. Eng.* **2020**, *15*, 8862827. [CrossRef]
25. Skarlatoudis, A.A.; Thio, H.K.; Somerville, P.G. Estimating shallow shear-wave velocity profiles in Alaska using the initial portion of P waves from local earthquakes. *Earthq. Spectra* **2022**, *38*, 1076–1102. [CrossRef]
26. Wu, Y.M.; Yen, H.Y.; Zhao, L.; Huang, B.S.; Liang, W.T. Magnitude determination using initial P waves: A single-station approach. *Geophys. Res. Lett.* **2006**, *33*, L05306. [CrossRef]

27. Li, N.; Huang, B.; Ling, D.S.; Wang, Q.J. Experimental research on behaviors of saturated loose sand subjected to oblique ellipse stress path. *Rock Soil Mech.* **2015**, *36*, 156.
28. Gu, C.; Cai, Y.Q.; Wang, J. Coupling effects of P-waves and S-waves based on cyclic triaxial tests with cyclic confining pressure. *Chin. J. Geotech. Eng.* **2012**, *34*, 1903–1909.
29. You, H.B.; Zhao, F.X.; Rong, M.S. Nonlinear seismic response of horizontal layered site due to inclined wave. *Chin. J. Geotech. Eng.* **2009**, *31*, 234–240.
30. Pan, D.G.; Lou, M.L.; Dong, C. Random wave-theory analysis of layered soil sites under P-wave and SV-wave excitation. *J. Eng. Mech.* **2006**, *23*, 66–71.
31. Sawazaki, K.; Snieder, R. Time-lapse changes of P-and S-wave velocities and shear wave splitting in the first year after the 2011 Tohoku earthquake, Japan: Shallow subsurface. *Geophys. J. Int.* **2013**, *193*, 238–251. [CrossRef]
32. Liu, Y.; Wu, R.S.; Ying, C.F. Scattering of elastic waves by an elastic or viscoelastic cylinder. *Geophys. J. Int.* **2000**, *142*, 439–460. [CrossRef]
33. Farra, V.; Pšenčík, I. Moveout approximations for P-and SV-waves in VTI mediaMoveout approximations in VTI media. *Geophysics* **2013**, *78*, WC81–WC92. [CrossRef]
34. Achenbach, J. *Wave Propagation in Elastic Solids*; Elsevier: Amsterdam, The Netherlands, 2012.
35. Xu, Z.D. *Seismic Wave Theory*; Tongji University Press: Shanghai, China, 1997.
36. Niu, B.H.; Sun, C.Y. *Half Space Medium and Seismic Wave Propagation*; Petroleum Industry Press: Beijing, China, 2002.
37. Wu, S.M. *Soil Dynamics*; China Architecture and Building Press: Beijing, China, 2000.
38. Kumari, P.; Sharma, V.K.; Modi, C. Reflection/refraction pattern of quasi-(P/SV) waves in dissimilar monoclinic media separated with finite isotropic layer. *J. Vib. Control.* **2016**, *22*, 2745–2758. [CrossRef]
39. Chattopadhyay, A.; Venkateswarlu, R.L.K.; Saha, S. Reflection of quasi-P and quasi-SV waves at the free and rigid boundaries of a fibre-reinforced medium. *Sadhana* **2002**, *27*, 613–630. [CrossRef]
40. Yoshimi, Y.; Tanaka, K.; Tokimatsu, K. Liquefaction resistance of a partially saturated sand. *Soils Found.* **1989**, *29*, 157–162. [CrossRef] [PubMed]
41. Yang, J. Reappraisal of vertical motion effects on soil liquefaction. *Geotechnique* **2004**, *54*, 671–676. [CrossRef]
42. Yang, J.; Sato, T. Interpretation of seismic vertical amplification observed at an array site. *Bull. Seismol. Soc. Am.* **2000**, *90*, 275–285. [CrossRef]
43. Ishihara, K.; Towhata, l. Sand response to cyclic rotation of principal stress directions as induced by wave loads. *Soils Found.* **1983**, *23*, 11–26. [CrossRef]
44. Allen, R.M.; Kanamori, H. The potential for earthquake early warning in southern California. *Science* **2003**, *300*, 786–789. [CrossRef]
45. Liu, H.; Zheng, T.; Bo, J. Statistical analysis of uncertainty for shear wave velocities of cohesive soils. *World Inf. Earthq. Eng.* **2010**, *26*, 99–103.
46. Miao, Y.; He, H.; Liu, H. Reproducing ground response using in-situ soil dynamic parameters. *Earthq. Eng. Struct. Dyn.* **2022**, *51*, 2449–2465. [CrossRef]
47. Wang, S.Y.; Zhuang, H.Y.; Zhang, H. Near-surface softening and healing in eastern Honshu associated with the 2011 magnitude-9 Tohoku-Oki Earthquake. *Nat. Commun.* **2021**, *12*, 1–10.